Chemical Science

ROYAL SOCIETY OF CHEMISTRY

EDGE ARTICLE

View Article Online
View Journal

Check for updates

Cite this: DOI: 10.1039/d6sc01794k

All publication charges for this article have been paid for by the Royal Society of Chemistry

Received 3rd March 2026
Accepted 9th April 2026

DOI: 10.1039/d6sc01794k

rsc.li/chemical-science

Lewis base-mediated stabilization of the lattice oxygen mechanism in RuO_2 for robust acidic water oxidation†

Sheng Hu,‡[a] Siyang Luo,‡[a] Haoxin Du,‡[a] Xiongfeng Zeng,‡[a] Jiao Yang,[b] Xing Wang, ‡*[a] Haifeng Bao‡*[a] and Na Yao ‡*[a]

Stabilizing the lattice oxygen oxidation mechanism (LOM) pathway of Ru-based oxygen evolution reaction (OER) electrocatalysts under acidic conditions is pivotal for efficient proton exchange membrane (PEM) water electrolysis. Herein, we propose a Lewis base regulation strategy by introducing In into RuO_2 to activate and stabilize the LOM process during the OER. Integrated *in situ* and *ex situ* characterization studies and theoretical calculations reveal that the In acts as an electron donor to modulate the interfacial water structure and accelerate deprotonation, thereby ensuring a continuous supply of *OH. Furthermore, In doping optimizes the electronic structure to promote *OH adsorption on Ru sites, enhance the Ru–O covalency, and stabilize oxygen vacancies generated during the LOM process, thereby synergistically improving both the activity and stability of the Ru-based catalyst along the LOM pathway. Benefiting from this Lewis base modulation, In-RuO_2 exhibits outstanding acidic OER performance, achieving 10 mA cm^{-2} at an overpotential of only 194 mV with excellent stability (>1000 h). Furthermore, In-RuO_2 outperforms RuO_2 in PEM electrolyzer tests, operating stably for over 1000 h at 1 A cm^{-2}. This work offers a design principle for highly active and stable LOM catalysts toward scalable green hydrogen production.

Introduction

Hydrogen production *via* water electrolysis driven by renewable energy sources represents a paradigmatic technology for generating green hydrogen, offering potential solutions to alleviate the current energy and environmental crises.[1–3] At present, proton exchange membrane (PEM) water electrolysis technology, characterized by its high efficiency, flexibility, and excellent compatibility with renewable energy sources, is emerging as a key driver in the advancement of the hydrogen economy.[4–6]. Nonetheless, the commercial viability of PEMWE technology remains challenged by the sluggish oxygen evolution reaction (OER) kinetics, requiring the utilization of both robust and efficient catalysts.[7–9] Despite the widespread application of IrO_2 in proton exchange membrane (PEM) water electrolyzers owing to its outstanding durability, the prohibitive cost and limited supply of iridium resources present major obstacles to large-scale commercialization.[10–12] Consequently, the development of alternative materials with high catalytic activity and reduced cost has emerged as a central focus of current research.

Among the potential candidates, RuO_2 stands out due to its relatively low overpotential and superior intrinsic activity. However, its poor long-term stability under acidic conditions, in sharp contrast to IrO_2, remains the primary bottleneck restricting its practical application.[13–15] Currently, emerging evidence suggests that RuO_2 tends to follow the lattice-oxygen-mediated mechanism (LOM) under OER conditions.[16–18] While this pathway enables accelerated reaction kinetics through energy barrier reduction, it inherently requires lattice oxygen involvement and generates oxygen vacancies (V_O), potentially disrupting the local electronic structure and damaging crystalline integrity.[19–21] This unstable effect will be significantly intensified under acidic conditions. Elevated concentrations of protons (H^+) in the electrolyte can strongly interact with Ru sites, promoting excessive oxidation (*e.g.*, $Ru^{4+} \rightarrow Ru^{5+} \rightarrow Ru^{7+}$) and destabilizing the surface electronic structure.[22] This phenomenon not only accelerates the formation and diffusion of lattice defects but also triggers the dissolution of Ru into high-valent, soluble species such as RuO_4 or RuO_5^{2-}, ultimately resulting in severe catalyst degradation.[23–25] In addition, the diminished availability of surface hydroxyl species (OH^-) in acidic media stemming from the high energy barrier for water activation hinders the timely replenishment of lattice oxygen,

---

[a] *State Key Laboratory of New Textile Materials and Advanced Processing, Wuhan Textile University, Wuhan 430200, P. R. China. E-mail: wx@wtu.edu.cn; baohaifeng@wtu.edu.cn; yaona@wtu.edu.cn*

[b] *College of Chemistry and Molecular Sciences, Wuhan University, Hubei 430072, Wuhan, P. R. China*

† Natural Science Foundation of Hubei Province (2025AFB860).

‡ Present address: No. 1 Sunshine Avenue, Jiangxia District, Wuhan, China.

thereby causing the accumulation of oxygen vacancies and further accelerating structural collapse. To address these challenges, constructing a local alkaline microenvironment around Ru sites by introducing electron-donating Lewis base (LB) species has emerged as a promising strategy.[26–28] Such species can act as proton scavengers, suppressing the overoxidation of Ru induced by H^+ and stabilizing oxygen vacancy intermediates formed during the LOM pathway. Nevertheless, a comprehensive understanding of rational design principles for such localized environments and their dual role in concurrently improving both structural stability and catalytic activity of RuO_2 catalysts in acidic media remains largely unexplored.

Building on this concept, we strategically introduced p-block elements (Al, Ga, and In) to establish a localized Lewis basic environment surrounding Ru sites by leveraging the distinctive s–p orbital coupling interactions between these elements and protons, configuring these elements to act as proton-targeted electron donors. Combined *in situ* and *ex situ* characterization studies along with density functional theory (DFT) calculations indicate that In, functioning as an enhanced Lewis base component during the OER process, establishes an electron-redistribution mechanism that inhibits the coupling between H^+ and Ru electrons, thereby suppressing excessive oxidation of Ru. Furthermore, In participates in charge compensation by balancing the local electronic perturbations caused by the formation of oxygen vacancies (V_O), thus stabilizing the V_O intermediates associated with the LOM pathway. In addition, the Lewis acid–base interaction between In and Ru modulates the structure and hydrogen bonding network of interfacial water within the electrical double layer (EDL). This enhances the concentration of free water molecules, accelerates water dissociation kinetics, and increases *OH coverage on the catalyst surface. Consequently, the continuous supply of reactants and rapid replenishment of lattice oxygen vacancies during the LOM are realized, synergistically improving the catalytic activity and durability. As a result, the synthesized In-RuO_2 catalyst exhibits an ultralow overpotential of approximately 193 mV to achieve 10 mA cm^{-2} in 0.5 M H_2SO_4. Moreover, when applied as the anode catalyst in a proton exchange membrane (PEM) electrolyzer, In-RuO_2 enables operation at 1 A cm^{-2} with a cell voltage of only 1.67 V and exhibits stable performance beyond 1000 h. This strategy provides a novel theoretical framework and design principle for enhancing the acid stability and long-term activity of Ru-based OER catalysts.

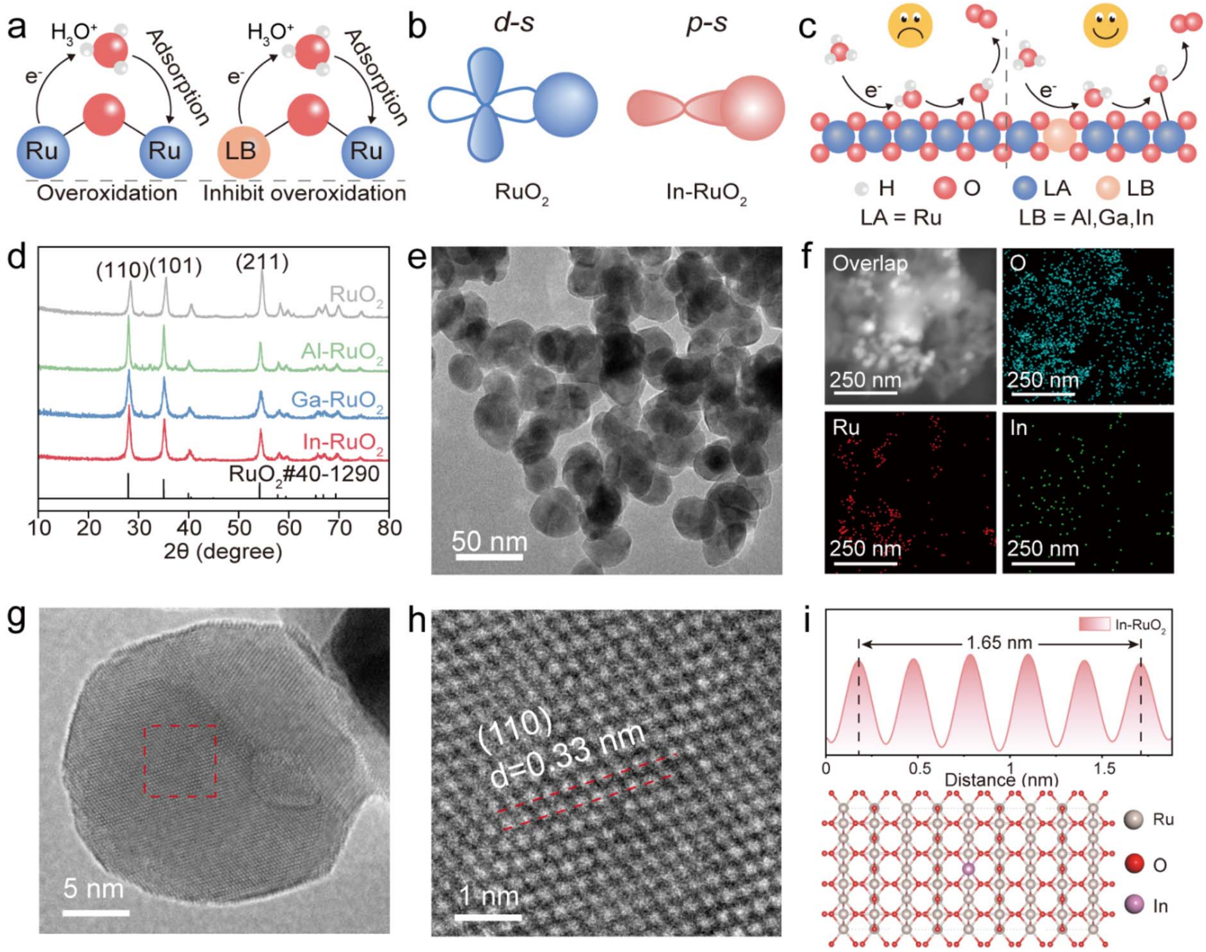

Fig. 1 Design and characterization of the RuO_2 based catalyst. (a–c) Overview of catalyst design for acidic OER. (d) XRD patterns of RuO_2 and M–RuO_2 (M = In, Al, Ga). (e) TEM image of In-RuO_2. (f) EDX elemental mapping of In-RuO_2 at a 250 nm scale. (g) HRTEM image of In-RuO_2. (h) Magnified HRTEM image of (g). (i) The simulated molecular structure of In-RuO_2.

Results and discussion

Synthesis and structural characterization

Under acidic conditions, the Ru sites undergo proton-induced electron ejection due to the attack of H^+, which subsequently leads to the over-oxidation of Ru (Fig. 1a). Theoretically, the electron transfer of this process mainly relies on the coupling between s and d orbitals. To effectively block the erosion path of H^+ on Ru sites, the most direct strategy is to introduce new p-orbital electron donors (Lewis base sites) near the Ru site.[29,30] By utilizing the lower orbital coupling energy barrier and stronger electronic cloud overlap associated with s–p orbital interactions, new electron transfer channels can be constructed (Fig. 1b). The Lewis acid–base pair synergy significantly suppresses electron dissipation at the Ru active sites, thereby maintaining an optimized charge distribution state in an acidic environment while simultaneously enhancing the OER activity and structural stability of the Ru-based catalyst (Fig. 1c).

Building on the above strategy, we prioritized the selection of p-block elements M (M = Al, Ga, or In) as the Lewis base component to construct Lewis acid–base pair systems (*i.e.* In–Ru), aiming to gain deep insights into their mechanistic role in enhancing OER performance. Specifically, the M doped RuO_2 (M–RuO_2) catalysts were prepared *via* homogeneously mixing the Ru and In precursors solutions, followed by calcination treatment. The X-ray diffraction (XRD) patterns of Al-RuO_2, Ga-RuO_2, In-RuO_2, and RuO_2 exhibit well-defined diffraction peaks that align with the characteristic rutile phase of RuO_2 (JCPDS No. 40-1290) (Fig. 1d). The structural morphology of the synthesized catalysts was examined through transmission electron microscopy (TEM) characterization. As illustrated in Fig. 1e and S1–S4, the In-RuO_2, Ga-RuO_2, Al-RuO_2 and RuO_2 catalysts consist of uniform nanoparticles with comparable size distributions. The energy-dispersive X-ray spectroscopy (EDX) mapping images reveal a uniform distribution of In, Ru and O in In-RuO_2, indicating that In atoms have been successfully incorporated into the RuO_2 lattice (Fig. 1f). Additionally, high-resolution transmission electron microscopy (HR-TEM) and the corresponding fast Fourier transform (FT) images of In-RuO_2 indicate a lattice fringe of 0.33 nm, which corresponds to the (110) plane of RuO_2 (Fig. 1g–i and S4).

To determine the chemical states of M-RuO_2 catalysts, X-ray photoelectron spectroscopy (XPS) and X-ray absorption spectroscopy (XAS) were utilized. As shown in Fig. 2a, the peak

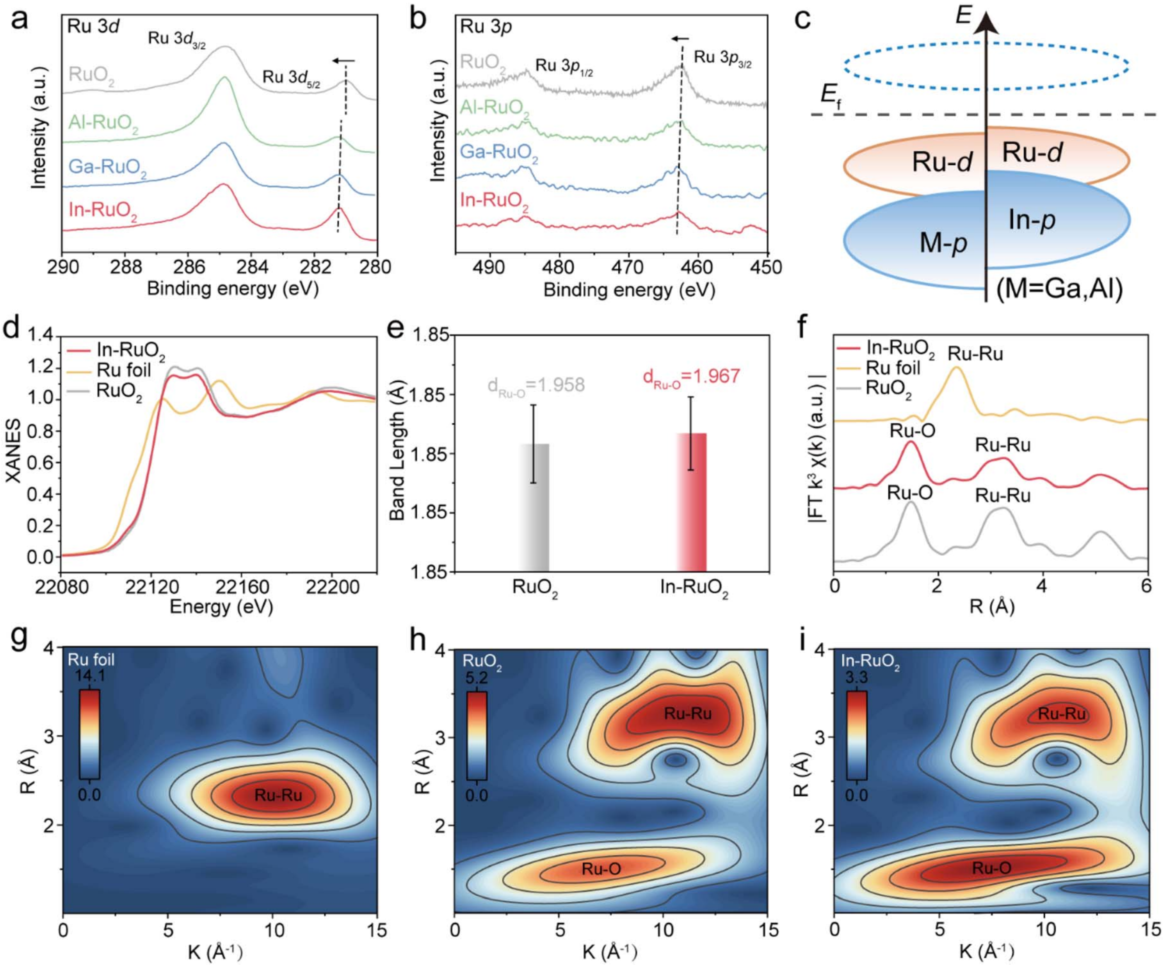

Fig. 2 Electronic structure characterization of RuO_2 and M–RuO_2. (a) Ru 3d XPS spectra. (b) Ru 3p XPS spectra. (c) Band structures of the compounds synthesized from M–RuO_2. (d) Ru K-edge XANES spectra. (e) Ru K-edge EXAFS fitting curves in *R* space for In-RuO_2. (f) Ru K-edge EXAFS spectra. (g–i) Wavelet transform for Ru K-edge EXAFS signals.

positions corresponding to Ru^{4+} in Ru $3d_{5/2}$ binding energy for In-RuO_2, Ga-RuO_2 and Al-RuO_2 exhibit positive shifts relative to RuO_2.[31–34] This trend is consistently observed in the Ru 3p spectra (Fig. 2b), suggesting that the introduction of Lewis basic elements (Al, Ga, and In) triggers directional electron transfer from the Ru center to the incorporated heteroatoms, thereby enabling these dopants to function as effective electron donors for H^+. Notably, comparative analysis reveals that the introduction of In induces a more pronounced electron transfer compared to Ga and Al, which can be attributed to In's stronger Lewis basicity and better energy level matching with Ru (Fig. 2c), making it more conducive to enhancing the interfacial charge redistribution during the interaction process. As a more effective electron donor, In substantially promotes electron interaction with H^+, thereby facilitating H_2O dissociation and accelerating the supply of *OH intermediates at Ru sites, ultimately enhancing the overall electrocatalytic activity and stability.[35] Furthermore, the high-resolution XPS spectra of Al 2p, Ga 2p and In 3d further indicate that Al, Ga and In were successfully incorporated into RuO_2 in their respective +3 oxidation states (Fig. S5). Additionally, in In-RuO_2, the intensity of the white-line peak at the Ru K-edge in the X-ray absorption near-edge structure (XANES) spectrum is slightly lower compared to that in RuO_2, indicating that In doping leads to a reduction in the local symmetry around Ru sites in RuO_2, thereby providing further evidence for the partial replacement of Ru sites by In atoms (Fig. 2d).[36,37] Notably, the Ru K-edge FT-EXAFS spectra display two distinct peaks, which are attributed to the first shell of Ru–O bonds and the second shell of M–O–Ru bonds, respectively (Fig. 2e–f).[38–40] Compared with the Ru–O bond length (1.96 Å) in RuO_2, the slight elongation (1.97 Å) observed in In-RuO_2 induces enhanced lattice oxygen activity (Fig. S6, 7 and Table S1), which is further supported by wavelet transform (WT) analysis of the EXAFS data, as shown in Fig. 2g–i, ultimately promoting acidic OER performance with an earlier onset potential.

Acidic OER performance

The acidic OER performances of the prepared catalysts were evaluated using a standard three-electrode system in a 0.5 M

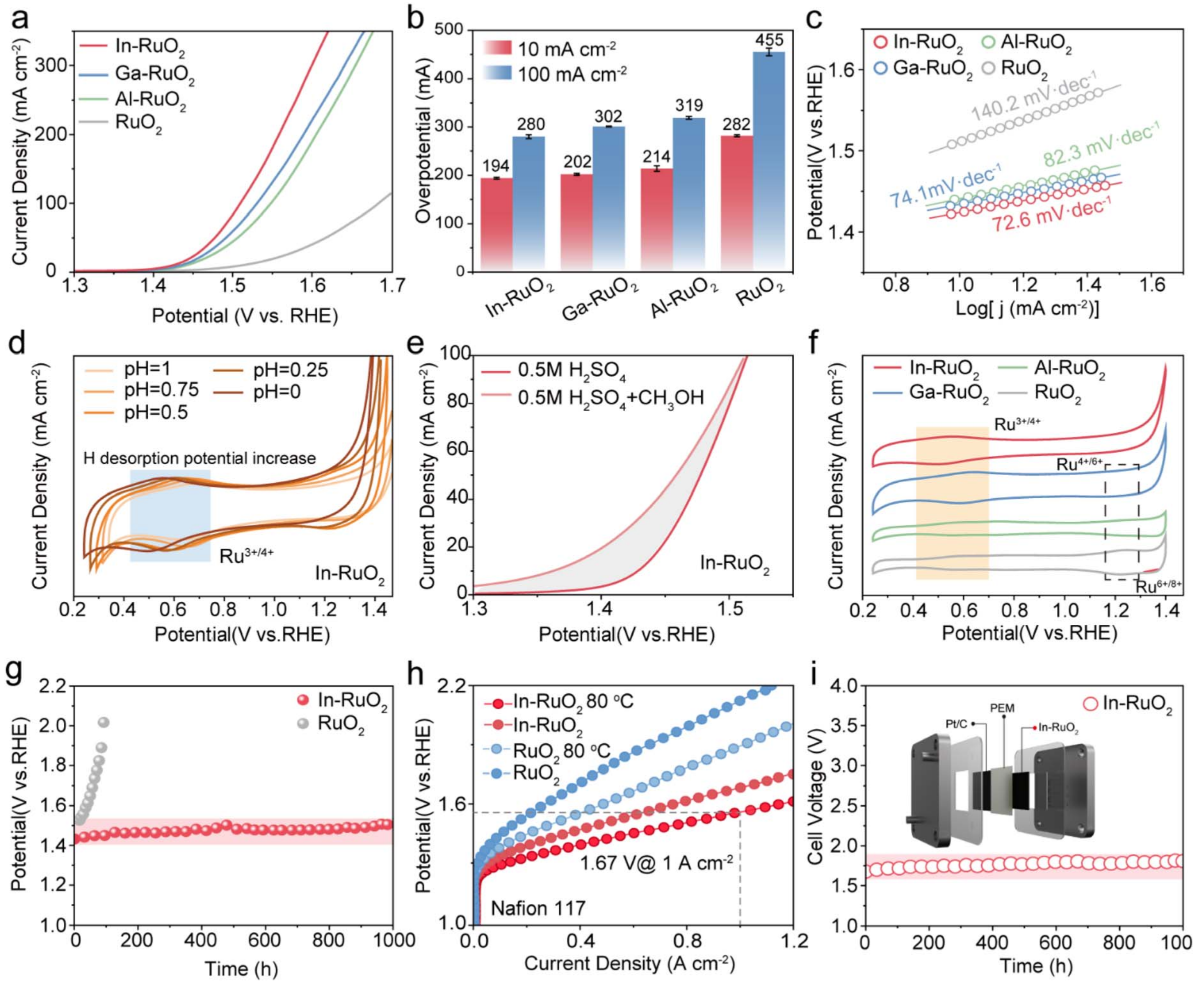

Fig. 3 OER performance measurements. (a) LSV curves of RuO_2 and M-RuO_2 in a 0.5 M H_2SO_4 solution. (b) The overpotentials at 10 mA cm^{-2} and 100 mA cm^{-2} of RuO_2 and M-RuO_2. (c) Corresponding Tafel plots according to the LSV curves in (a). (d) pH-dependent test of In-RuO_2. (e) LSV curves for In-RuO_2 in 0.5 M H_2SO_4 with and without methanol (0.5 M). (f) CV analysis of the redox peaks of RuO_2 and M-RuO_2. (g) Chronopotentiometric curves of RuO_2 and In-RuO_2 at a current density of 10 mA cm^{-2}. (h) LSV curves of the PEMWEfor RuO_2 and In-RuO_2 at 25 and 80 °C. (i) Durability cell voltage–time plots for the PEMWE at a constant current density of 1 A cm^{-2} for 1000 h.

H_2SO_4 electrolyte. All potential values were adjusted to the reversible hydrogen electrode (RHE) scale for calibration. Linear sweep voltammetry (LSV) curves presented in Fig. 3a and S8 indicate that In-RuO_2 exhibits enhanced OER performance compared to other samples. To reach a current density of 10 mA cm^{-2}, In-RuO_2 requires an overpotential of 194 ± 2 mV, significantly lower than that of RuO_2 (282 ± 2 mV), Al-RuO_2 (214 ± 6 mV) and Ga-RuO_2 (202 ± 2 mV) (Fig. 3b).

Moreover, the reaction kinetics of M-RuO_2 were evaluated from the Tafel slope derived from polarization curves, as shown in Fig. 3c. In-RuO_2 exhibits a Tafel slope of 72.6 mV dec^{-1}, demonstrating its superior electrochemical kinetics compared to Al-RuO_2 (82.3 mV dec^{-1}), Ga-RuO_2 (74.1 mV dec^{-1}), and RuO_2 (140.2 mV dec^{-1}). This is further evidenced by the smaller charge transfer resistance (R_{ct}) value at 1.5 V *vs.* RHE for In-RuO_2 from *operando* electrochemical impedance spectra (EIS) (Fig. S9 and 10). Then combining the Bode phase plot analysis, while In-RuO_2 exhibits a comparable behavior to other catalysts in the low-frequency region (electron transfer responses at the catalyst–electrolyte interface), its phase angle in the high-frequency region (electron transfer responses at the catalyst layer) decreases more rapidly with the increase of the potential (Fig. S11 and 12).[41] This indicates that the accelerated electron transfer response of In-RuO_2 within the catalyst layer promotes more efficient reaction kinetics, thereby enhancing OER activity. To further evaluate the intrinsic activity of In-RuO_2, the turnover frequency (TOF) and electrochemically active surface area (ECSA) were calculated. Notably, In-RuO_2 exhibits a TOF value of 0.518 s^{-1} among M-RuO_2 at 1.55 V *vs.* RHE, which is about 10 times higher than that of RuO_2 (0.055 s^{-1}), indicating its higher intrinsic OER activity (Fig. S13). The double-layer capacitance (C_{dl}), a key parameter for estimating the ECSA, was experimentally characterized to assess intrinsic catalytic activity (Fig. S14). As depicted in Fig. S15, the C_{dl} value of In-RuO_2 is determined to be 72.4 mF cm^{-2}, which exceeds the values of Al-RuO_2 (51.3 mF cm^{-2}), Ga-RuO_2 (61.4 mF cm^{-2}), and RuO_2 (36.3 mF cm^{-2}), suggesting a higher availability of active surface sites for the OER process. Moreover, the ECSA-normalized OER activity of In-RuO_2 is consistently superior to that of Al-RuO_2, Ga-RuO_2, and RuO_2, confirming its exceptional intrinsic acidic OER activity (Fig. S16). Furthermore, the H_2 desorption potential of In-RuO_2 shifts significantly to more positive direction as the pH value of the electrolyte increases (Fig. 3d and S17). This indicates that the incorporation of In with stronger Lewis basicity markedly enhances the catalyst's ability to promote water dissociation, thereby increasing the coverage of *OH on the catalyst surface.[17,25] To further quantify the surface coverage of *OH intermediates, methanol was employed as a molecular probe, leveraging the methanol oxidation reaction (MOR), wherein methanol acts as a nucleophile to selectively react with electrophilic *OH groups adsorbed on the catalyst surface.[42,43] Experimental results show that upon introducing 1.0 M methanol into a 0.5 M H_2SO_4 solution, both M-RuO_2 and RuO_2 exhibit a significant increase in current density, attributed to the electrooxidation of methanol (Fig. 3e and S18). The current density difference resulting from the MOR was quantified by integrating the area enclosed between the polarization curves, as this area correlates directly with the quantity of transferred charges. A greater current difference between the MOR and OER is observed for In-RuO_2 compared to Al-RuO_2, Ga-RuO_2 and RuO_2, suggesting a higher capability for *OH compensation on In-RuO_2, which contributes to enhanced OER activity and stability. The O 1s XPS spectra investigations also reveal a higher abundance of *OH (~531.8 eV) on the In-RuO_2 catalyst compared to that of Al-RuO_2, Ga-RuO_2 and RuO_2, which is consistent with the MOR results (Fig. S19 and Table S2). Then, cyclic voltammetry (CV) analysis of M-RuO_2 and RuO_2 was conducted at a scan rate of 1 mV s^{-1} to investigate the oxidation behavior of Ru sites at high potentials. Three distinct redox peaks can be observed in RuO_2, Al-RuO_2 and Ga-RuO_2 located at approximately 0.64, 1.23 and 1.36 V, which can be attributed to Ru^{3+}/Ru^{4+}, Ru^{4+}/Ru^{6+} and Ru^{6+}/Ru^{8+} transitions, respectively.[44] In contrast, no characteristic peaks corresponding to Ru^{4+}/Ru^{6+} and Ru^{6+}/Ru^{8+} are detected in the In-RuO_2 sample (Fig. 3f), indicating that the introduction of In suppresses the electron-donating behavior of Ru and thereby inhibits the formation of high-valence Ru^{n+} ($n > 4$) species, leading to improved OER stability. Then, the long-term operational stability of In-RuO_2 under acidic conditions was validated *via* chronopotentiometric stability testing and extended CV cycling. As expected, In-RuO_2 demonstrates almost no significant decay in the LSV curves before and after 2000 cycles of CV testing (Fig. S20a). By contrast, the RuO_2 electrocatalyst exhibits a notable rise in overpotential (Fig. S20b). Moreover, the stability of In-RuO_2 and RuO_2 was evaluated through chronoamperometric measurements conducted at a current density of 10 mA cm^{-2}, demonstrating that In-RuO_2 exhibited stable operation for over 1000 h, whereas RuO_2 exhibits rapid performance degradation under identical conditions (Fig. 3g). Evaluations of the activity and stability of In-RuO_2 were also conducted relative to recently reported Ru-based catalysts, demonstrating its better performance than the majority of the Ru-based catalysts reported to date (Table S3). Inductively coupled plasma mass spectrometry (ICP-MS) was further performed to quantify the dissolution rates of Ru. As illustrated in Fig. S21and 22 and Table S4, In-RuO_2 demonstrates exceptionally low dissolution rates of 0.38% for Ru after 60 h of stability testing, with the stability number (*S*-number) determined to be 3.18×10^5 at 60 h, indicating its excellent activity and long-term durability. Besides, the outstanding structural robustness of In-RuO_2 is further demonstrated by the XPS and XRD spectra after the OER, which are consistent with those observed before the OER (Fig. S23 and 24).

Capitalizing on the overall high activity and stability of In-RuO_2 for the OER, we integrated In-RuO_2 as the anode catalyst, commercial Pt/C as the cathode catalyst and a proton exchange membrane (Nafion 117) to construct a membrane electrode assembly (MEA) and further used it to assemble a PEMWE (Fig. S25). As illustrated in Fig. 3h, for the In-RuO_2‖ Pt/C electrolyzer, to achieve a water electrolysis current density of 1.0 A cm^{-2}, the required voltages are only 1.78 V (room temperature) and 1.67 V (80 °C), respectively, demonstrating markedly lower overpotentials compared to the benchmark RuO_2‖Pt/C electrolyzer under identical operating conditions.

Moreover, the In-RuO_2‖Pt/C electrolyzer exhibits remarkable stability, retaining operation at 1.0 A cm^{-2} for over 1000 h with only a minimal cell voltage increase of 7.6%, suggesting that the In-induced enhancement of *OH coverage greatly boosts both the activity and stability of RuO_2 under realistic operating conditions (Fig. 3i). The performance of the In-RuO_2-based PEMWE challenges the established views on the durability limits of Ru-based catalysts while rivaling the performance of reported Ru-based catalysts (Table S5), highlighting its potential for sustainable hydrogen production.

Mechanistic investigation of acidic OER

Electrochemical and *in situ* spectroscopic techniques were employed to further investigate the catalytic mechanism of In-RuO_2, as well as to elucidate the specific roles of In and Ru sites. As shown in Fig. 4a and S26, the LSV curves for M-RuO_2 and RuO_2 in H_2SO_4 solution (pH 0–1) were measured at a scan rate of 5 mV s^{-1}. All the M-RuO_2 and RuO_2 samples exhibit significant pH dependence, indicating nonconcerted proton–electron transfer processes for the lattice oxygen mechanism (LOM) (Fig. 4b). A tetramethylammonium cation (TMA^+) probe experiment was conducted to investigate the potential presence of O_2^{2-} species during the OER process of M-RuO_2 and RuO_2, leveraging its specific sensitivity to these negatively charged O_2^{2-} species derived from the LOM pathway.[45] The result demonstrates an obvious difference in the LSV curves of the samples with and without TMA^+, revealing the existence of O_2^{2-} species during the OER process, and confirms the involvement of the LOM pathway for these catalysts (Fig. 4c and S27). Subsequently, *in situ* attenuated total reflection surface-enhanced infrared absorption spectroscopy (ATR-SEIRAS) was employed to confirm the unique LOM process (Fig. 4d). An obvious potential-dependent peak emerges at ~1200 cm^{-1} across all catalysts, attributable to the stretching vibration of the *OO intermediate, confirming the reaction pathway consistent with the LOM (Fig. 4e and S28).[46] Notably, the dynamic *OO absorption band emerges at a lower voltage (~1.1 V) for In-RuO_2 compared to Al-RuO_2, Ga-RuO_2, and RuO_2, which contributes to the lower overpotential of In-RuO_2. ^{18}O-labeled *in situ* differential electrochemical mass spectrometry (DEMS) measurement was carried out to elucidate the OER mechanism associated with In-RuO_2 and RuO_2 (Fig. S29). RuO_2 and In-RuO_2 were initially subjected to three LSV cycles in 0.5 M H_2SO_4

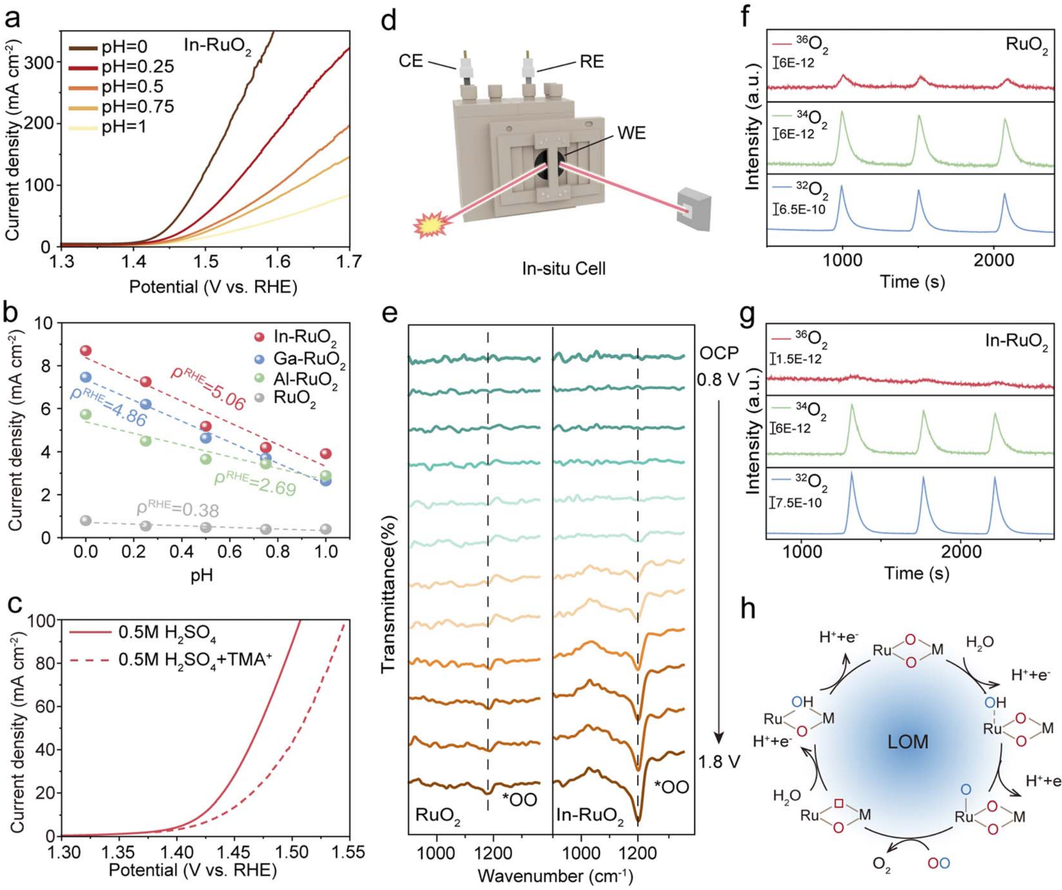

Fig. 4 OER performance measurements. (a) LSV curves of In-RuO_2 in electrolyte with different pH values. (b) The linear relationship of current density *vs.* pH. (c) OER polarization curves of In-RuO_2 in 0.5 M H_2SO_4 electrolyte with and without TAM^+. (d) *In situ* ATR-SEIRAS device diagram. (e) *In situ* ATR-SEIRAS spectra. (f and g) DEMS signals of $^{32}O_2$ [$^{16}O^{16}O$, mass/charge ratio (*m*/*z*) = 32], $^{34}O_2$ ($^{16}O^{18}O$, *m*/*z* = 34), and $^{36}O_2$ ($^{18}O^{18}O$, *m*/*z* = 36) from the reaction products for ^{18}O-labelled RuO_2 and In-RuO_2 catalysts in $H_2{}^{16}O$/0.5 M H_2SO_4 electrolyte. (h) Schematic illustration of the LOM.

prepared with $H_2{}^{18}O$ as the solvent to isotopically label the catalysts. Subsequently, the ^{18}O-labeled catalysts were rinsed with pure water to remove the adsorbed $H_2{}^{18}O$ before being cycled in 0.5 M H_2SO_4 solution prepared with $H_2{}^{16}O$. As depicted in Fig. 4f–g, In-RuO_2 and RuO_2 produce $^{32}O_2$ and $^{34}O_2$, as well as trace amounts of the $^{36}O_2$ product, further confirming their participation in the LOM pathway.[47–49] Therefore, the introduction of the Lewis basic element (In) sustains the LOM pathway, as depicted in Fig. 4h.

To further verify the *OH compensation capability and the replenishment of lattice oxygen, an in-depth analysis of *in situ* Raman and ATR-SEIRAS data was performed. The hydrogen-bond network within the electrical double-layer governs water adsorption/dissociation and proton transfer during acidic OER, where theoretical studies reveal reduced water dissociation energy with weaker hydrogen bonding, while exhibiting enhanced proton transfer with stronger bonding.[50,51] This interplay necessitates precise regulation of interfacial water availability and activity to optimize OER performance. *In situ* ATR-

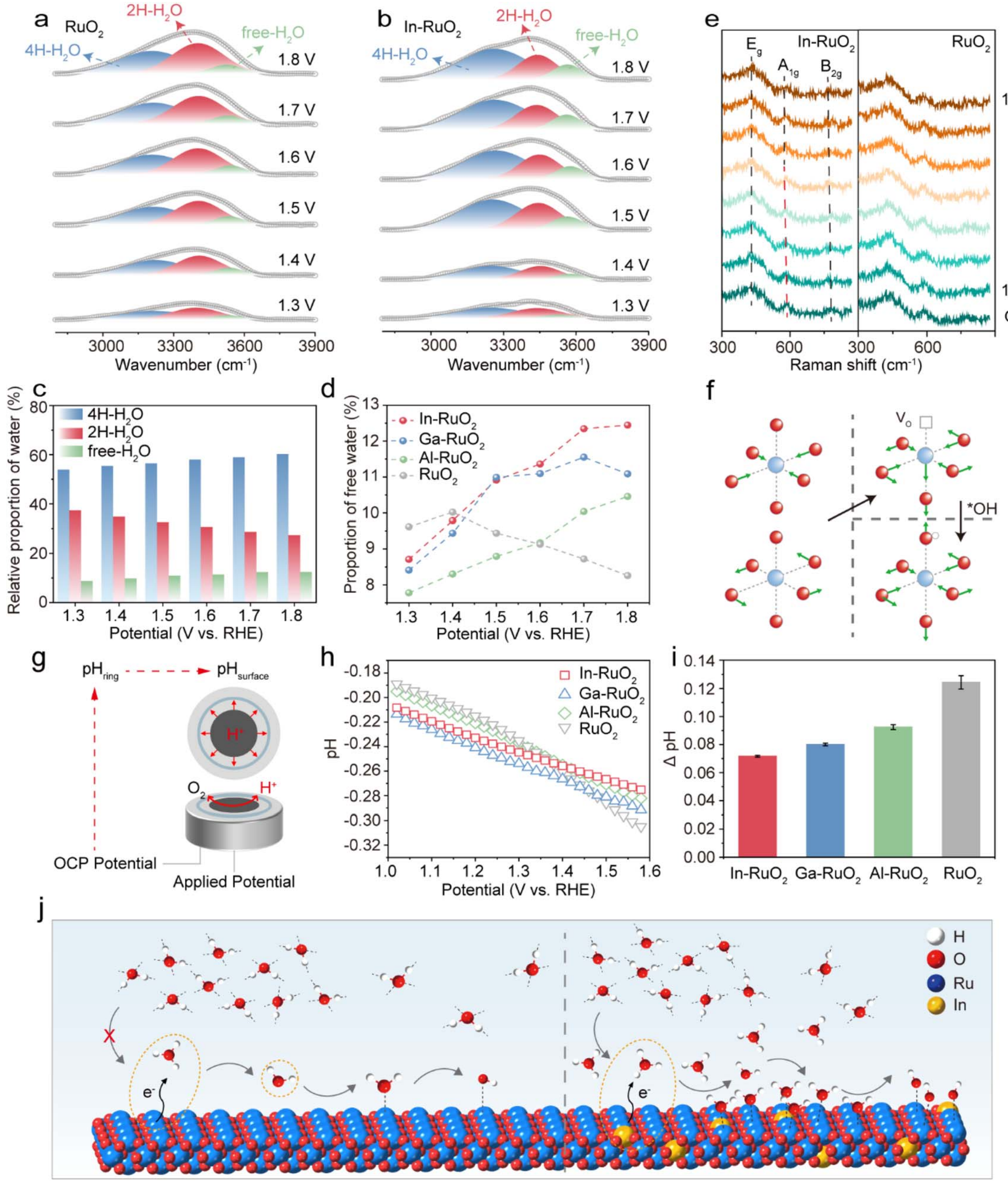

Fig. 5 *In situ* Raman spectra were recorded at potentials from 1.3 to 1.7 V on (a) RuO_2 and (b) In-RuO_2. (c) Percentage of various types of interfacial water structures at applied potential in In-RuO_2. (d) The proportion of free water in RuO_2 and In-RuO_2 at different potentials. (e) *In situ* Raman spectra of RuO_2 and In-RuO_2 during the OER. (f) *In situ* Raman spectra of RuO_2 and In-RuO_2 during the OER. (g) Schematic illustration of local pH monitoring using a rotating ring-disk electrode (RRDE). (h and i) Changes in the local pH on M-RuO_2 and RuO_2 electrodes at OER potentials in 0.5 M H_2SO_4 and their variations. (j) Schematic representation of the electrochemical interface of RuO_2 and In-RuO_2 during the OER.

SEIRAS was performed to monitor the behavior of interfacial water during the OER at various applied potentials. Wavenumbers ranging from 3000 to 3600 cm^{-1} are attributed to the OH stretching mode. Three peaks located at about 3200, 3400 and 3600 cm^{-1} are assigned to the 4-coordinated hydrogen-bonded water (4-HB-H_2O), 2-coordinated hydrogen-bonded water (2-HB-H_2O), and free-H_2O with weak hydrogen-bond interactions, respectively (Fig. 5a, b, S30 and Tables S6–9).[51–53] For all catalysts, 4-HB-H_2O consistently dominates across the full range of detected potentials, facilitating efficient proton transfer during the acidic OER process.[54] Upon increasing the voltage, a gradual rise in the proportion of free-H_2O is observed for M-RuO_2, with In-RuO_2 exhibiting the most pronounced increase, followed by Ga-RuO_2 and Al-RuO_2, while RuO_2 shows an opposing trend (Fig. 5c and d). This phenomenon can be attributed to the introduction of the Lewis basic element, which enhances the electron donation ability of the catalyst toward H^+, thereby effectively regulating the electronic environment of interfacial water molecules. Consequently, the aqueous structure undergoes a dynamic shift from stable bound water to more active free water, thereby continuously replenishing the water consumed during the acidic OER process and maintaining the continuity and activity of the interfacial processes. In addition, the *in situ* Raman spectra presented in Fig. 5e and S31 reveal the characteristic signals at approximately 450 cm^{-1}, 610 cm^{-1}, and 700 cm^{-1}, corresponding to the E_g, A_{1g}, and B_{2g} modes of RuO_2, respectively.[55] As the potential increases to 1.3 V, the E_g and A_{1g} peaks in In-RuO_2 exhibit a distinct blueshift, originating from the Ru–O bond elongation caused by the formation of oxygen vacancy intermediates during the LOM process (Fig. 5f).[20] With a further increase in potential, the Raman shifts of these peaks stabilize, a behavior not observed in RuO_2, which can be attributed to the rapid replenishment of lattice oxygen in In-RuO_2, thereby establishing a stable catalytic cycle. Notably, the continuous intensity enhancement of the asymmetric B_{2g} mode Raman peak with increasing potential, a feature not observed in RuO_2, provides compelling evidence for the rapid compensation of *OH. To quantitatively evaluate the influence of introducing Lewis base moieties on interfacial proton transport behaviour, a rotating ring-disk electrode (RRDE) technique was employed (Fig. 5g) to *in situ* monitor the local pH evolution at the surface of the M-RuO_2 (M = In, Ga, Al) electrode at different applied potentials in 0.5 M H_2SO_4 (bulk pH = 0.89), with RuO_2 for comparison (Fig. S32–S34). Based on the RRDE measurements, the M-RuO_2 and RuO_2 electrodes exhibit identical initial local pH values, which are comparable to that of the bulk electrolyte. Upon reaching the onset potential of the OER, a decrease in the local pH is observed for all catalysts, primarily due to proton generation at the electrode–electrolyte interface during the OER process (Fig. S32). Notably, given that the OER proceeds *via* a proton-coupled electron transfer (PCET) mechanism, In-RuO_2 simultaneously exhibits accelerated deprotonation kinetics accompanied by a more moderate decrease in interfacial pH (Fig. 5h, S33 and 34). Specifically, at the same applied potential (*e.g.*, 1.7 V *vs.* RHE), In-RuO_2 delivers a higher OER current density than other M-RuO_2 catalysts and pristine RuO_2, while showing a smaller extent of local pH reduction (Fig. 5i), collectively indicating significantly enhanced interfacial deprotonation kinetics for In-RuO_2.[56] Based on the above analysis, incorporation of the Lewis basic element (In) markedly enhances the catalyst's electron donation capability toward interfacial water, thereby modulating the electronic environment of water molecules and promoting the structural transition from bound to a more reactive free state (Fig. 5j). This transformation facilitates more efficient water dissociation and elevates the accumulation of *OH intermediates on Ru sites, thereby improving the dynamic replenishment of lattice oxygen during the LOM process and ultimately enhancing both the catalytic activity and stability of RuO_2.

Theoretical insights into intrinsic activity and stability

To elucidate the mechanistic origins underlying the enhanced activity and stability of In-RuO_2 relative to other M-RuO_2 (M = Al, Ga) and RuO_2, density functional theory (DFT) calculations were employed to probe the local electronic environment. The corresponding computational models are depicted in Fig. 6a–b and S35 (see the Methods section for computational details). Two-dimensional electron localization function (ELF) analyses demonstrate that the substitution of Ru with In induces a local redistribution of electron density that augments Ru–O orbital hybridization, thereby elevating Ru–O bond covalency as well as promoting lattice oxygen activity (Fig. 6c, d and S36). Furthermore, Bader charge analysis indicates that In doping leads to electron delocalization at Ru sites, resulting in an increased oxidation state (Fig. 6e and S37), and thus enhancing the adsorption affinity of Ru sites toward oxygen intermediates, which is highly consistent with the XPS results. Concurrently, the In sites accumulate electron density and function as Lewis bases, thus tending to serve as an electron donor for H^+, facilitating the transformation of stable H_3O^+ into free H_2O configuration. This is further corroborated by the solvation models and ELF results, as presented in Fig. 6f, S38 and S39. This accelerates H_2O dissociation, thereby ensuring a sufficient supply of *OH and facilitating the rapid replenishment of lattice oxygen within the LOM pathway. Moreover, the partial density of states (PDOS) analysis reveals an upshift in the Ru-d band center following In incorporation (Fig. 6g, h and S40), which strengthens the adsorption of oxygen intermediates at Ru sites. Meanwhile, the energy gap between Ru-d and O-p states gradually decreases with increasing In doping, providing further evidence for the enhanced reactivity of lattice oxygen. Additionally, charge density difference results confirm that *OH adsorption is enhanced in the In-RuO_2 system (Fig. S41). The results further indicate that In carries more negative charge, making the H in *OH more prone to electron exchange with In (Fig. 6i and j), thereby accelerating the interfacial electron transfer process. Projected crystal orbital Hamilton population (pCOHP) analysis further demonstrates the strengthened bonding interaction between In and H (Fig. 6k and l), which is consistent with the aforementioned findings. As expected, In doping facilitates the deprotonation process, significantly lowering the energy barrier of the rate determining step (RDS) in the LOM pathway to 1.40 eV, thus boosting OER activity (Fig. 6m and S42). In addition, In doping effectively

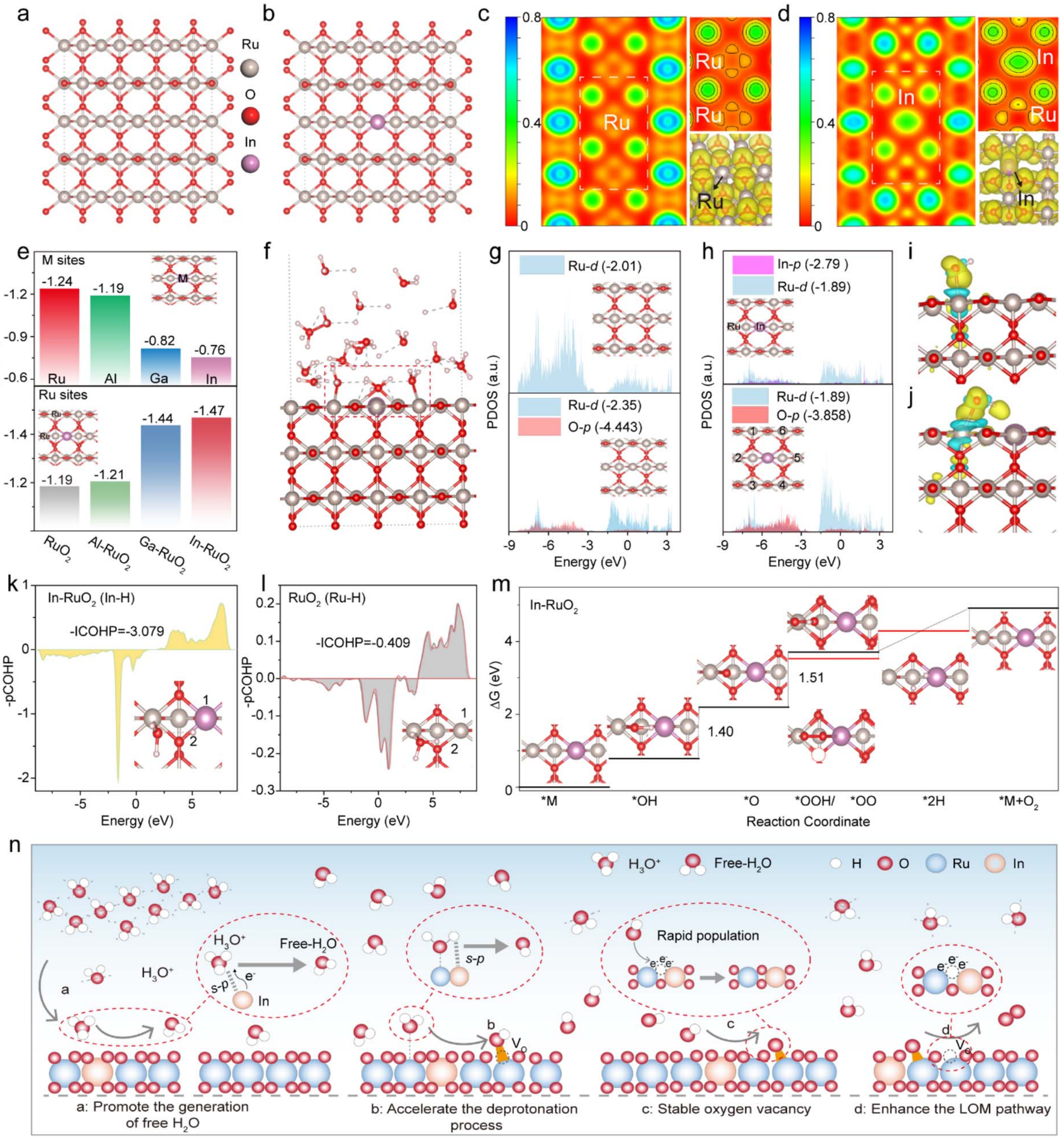

Fig. 6 DFT calculations. The geometric configurations of (a) RuO_2 and (b) In-RuO_2. The two-dimensional electron localization function (ELF) maps of (c) RuO_2 and (d) In-RuO_2, revealing the degree of electron localization around different atomic species. (e) The Bader charge analysis for M-RuO_2. (f) The solvation model of In-RuO_2. The PDOS of (g) RuO_2 and (h) In-RuO_2. Differential charge density for (i) RuO_2 and (j) In-RuO_2. The integrated COHP (ICOHP) analyses of M–H bonds in (k) In-RuO_2 and (l) RuO_2. (m) Free energy profiles of different OER intermediates of In-RuO_2. (n) Schematic illustration of dynamic evolution of interfacial water molecules on the surface of In-RuO_2.

redistributes the charge imbalance caused by oxygen vacancy (Vo) formation in the LOM pathway, which alleviates local structural distortion and instability associated with Vo generation, thereby enhancing the structural integrity and electrochemical durability of RuO_2 during the OER (Fig. S43). Overall, the enhanced OER performance of In-RuO_2 can be attributed to the following factors: (i) as a Lewis base, In facilitates the transformation of H_3O^+ configurations into free water, which accelerates water dissociation and *OH supply, expedites deprotonation and lowers the kinetic barrier of the LOM pathway. (ii) The incorporation of In not only strengthens oxygen species adsorption at Ru sites and enhances the Ru–O bond covalency, but also mitigates the charge imbalance caused by V_O formation, thereby suppressing Ru dissolution during the LOM process and ultimately improving the catalytic activity and stability (Fig. 6n).

Conclusions

In summary, we propose an innovative strategy involving the incorporation of Lewis base element In into the RuO_2 lattice to promote and stabilize the LOM pathway during the acidic OER process. By integrating multiple *in situ* characterization studies with theoretical calculations, we reveal that In doping modulates the interfacial water structure and increases the proportion of free water, thereby facilitating water dissociation and ensuring continuous supply of *OH intermediates to maintain high surface coverage. The electron effect induced by In accelerates the deprotonation process and decreases the energy barrier of the rate-determining step in the LOM pathway, thus significantly enhancing the OER activity. Furthermore, In incorporation not only strengthens the oxygen intermediate adsorption at Ru sites and increases the Ru–O bond covalency to boost intrinsic activity, but also effectively mitigates the charge imbalance caused by Vo to enhance the stability. Benefiting from this unique Lewis base regulation strategy, In-RuO_2 not only successfully resolves the inherent stability issue of the LOM pathway but also remarkably boosts OER activity. The catalyst exhibits outstanding acidic OER performance, requiring only an overpotential of 194 mV to achieve a current density of 10 mA cm^{-2} and exhibiting excellent durability. Furthermore, it demonstrates superior PEM electrolyzer performance, stably operating at a low cell voltage of only 1.67 V at 1 A cm^{-2} for over 1000 h. This work provides a rational design principle for optimizing LOM-mediated Ru-based catalysts, establishing a solid foundation for developing highly efficient catalytic systems for large-scale green hydrogen production.

Author contributions

S. H. conducted the experiments and collected the data. S. L., H. D. and X. Z. assisted in data collection. J. Y. assisted in analyzing the data. X. W. designed the experimental schemes, performed conceptualization, analyzed the data, wrote the draft, and performed review & editing. H. B. supervised the work. N. Y. carried out the DFT calculations, wrote the draft, and performed review & editing. All authors took part in the discussion of data and gave comments on the manuscript.

Conflicts of interest

There are no conflicts to declare.

Data availability

The data supporting this article have been included as part of the supplementary information (SI). Supplementary information: experimental and theoretical details as well as additional characterization and performance data. See DOI: https://doi.org/10.1039/d6sc01794k.

Acknowledgements

This work was financially supported by the National Natural Science Foundation of China (22309137 and 22279095), the Department of Science and Technology of Hubei Province (2024CSA076; 2025AFB860), and the Hubei Key Laboratory for New Textile Materials and Applications Research (FZXCL202206). We acknowledge the great help from Prof. Weilin Xu and coworkers at Wuhan Textile University for helpful measurements and discussion. We thank the Analytical and Testing Center of Wuhan Textile University for the XRD, XPS and Raman tests.

References

1 C. Qiu, C. Sellers, Z.-Y. Wu, D. A. Cullen, E. Stavitski, A. Tayal, T.-U. Wi, M. Kodali, B. Erb, A. Smeltz, F.-Y. Chen, Y. Feng, Z. Yu, A. Elgazzar, T. Terlier, T. P. Senftle and H. Wang, *Nat. Nanotechnol.*, 2025, **20**, 1787–1795.
2 H. Xie, Z. Zhao, T. Liu, Y. Wu, C. Lan, W. Jiang, L. Zhu, Y. Wang, D. Yang and Z. Shao, *Nature*, 2022, **612**, 673–678.
3 S. Li, L. Deng, S. F. Hung, S. Zhao, L. Wang, Y. Hao, Y. Long, B. Li, Y. H. Hsu, Y. Y. Chen, Y. Zhang, T. Y. Chen, F. Hu, L. Li, Y. Hu, Y. Wu and S. Peng, *Adv. Mater.*, 2025, **38**, e07340.
4 J. Chen, Y. Ma, C. Cheng, T. Huang, R. Luo, J. Xu, X. Wang, T. Jiang, H. Liu, S. Liu, T. Huang, L. Zhang and W. Chen, *J. Am. Chem. Soc.*, 2025, **147**, 8720–8731.
5 Y. Wang, H. Yan and H. Fu, *eScience*, 2025, **5**, 100323.
6 C. Wei, C. Liu, Z. Zhang, K. Sun, C. Xing, W. Shi, Y. Li, J.-F. Li and B. Zhang, *Joule*, 2025, **9**, 102058.
7 M. Y. Lin, W. J. Li, H. Y. Lin, S. Dai, Z. X. Lou, J. C. Wu, H. Q. Fu, S. R. Fang, H. Fan, X. X. Mao, X. Q. Chen, H. Y. Yuan, P. F. Liu, H. G. Yang and Y. Hou, *Energy Environ. Sci.*, 2025, **18**, 9183–9193.
8 W. Li, J. Lv, X. Chen, B. Wang and L. Wang, *J. Am. Chem. Soc.*, 2025, **147**, 29505–29516.
9 D. Simondson, M. F. Tesch, I. Spanos, T. E. Jones, J. Guo, B. V. Kerr, M. Chatti, S. A. Bonke, R. Golnak, B. Johannessen, J. Xiao, D. R. MacFarlane, R. K. Hocking and A. N. Simonov, *Nat. Energy*, 2025, **10**, 1013–1024.
10 S. R. Fang, H. X. Yang, H. Y. Lin, M. Y. Lin, F. X. Mao, H. Fan, H. Q. Fu, H. Y. Yuan, C. Sun, P. F. Liu and H. G. Yang, *Energy Environ. Sci.*, 2025, **18**, 5470–5481.
11 K. H. Park, Y. Lim, H. B. Bae, J. S. Kim, S. Lee, D. Kim and S.-Y. Chung, *J. Am. Chem. Soc.*, 2025, **147**, 17725–17738.
12 R. Qin, G. Chen, X. Feng, J. Weng and Y. Han, *Adv. Sci.*, 2024, **11**, 2309364.
13 Y. Yang, S. Wang, G. Zhang, X. Li, Q. Wu, H. Liu, Z. Deng, X. Han, S. Zhang, W. Dong, J. Song, Y. Chen, X. Gao, Y. Yang, J. Dong, L. Cao and Z. Zhao, *Angew. Chem., Int. Ed.*, 2025, **64**, e202512848.
14 Z. Wang, M. Wang, X. Li, H. Huang, X. Sun, J. Feng, S. Liu, H. Luo, L. Li, X. Zou and X. Zhao, *Nano Lett.*, 2025, **25**, 13267–13275.
15 X. Cao, L. Miao, W. Jia, H. Qin, G. Lin, R. Ma, T. Jin and L. Jiao, *Nat. Commun.*, 2025, **16**(16), 6217.
16 L. Wang, S.-F. Hung, S. Zhao, Y. Wang, S. Bi, S. Li, J.-J. Ma, C. Zhang, Y. Zhang, L. Li, T.-Y. Chen, H.-Y. Chen, F. Hu, Y. Wu and S. Peng, *Nat. Commun.*, 2025, **16**(16), 3502.
17 Q. Lu, J. Liu, X. Zou, B. Huang, W. Wu, J. Yin, Z. Q. Liu and Y. Wang, *Angew. Chem., Int. Ed.*, 2025, **64**, e202503733.
18 Y. Liu, Y. Wang, H. Li, M. G. Kim, Z. Duan, K. Talat, J. Y. Lee, M. Wu and H. Lee, *Nat. Commun.*, 2025, **16**(16), 1717.

19 S. Li, S. Zhao, S.-F. Hung, L. Deng, L. Wang, F. Shi, A. Dong, Y. Zhang, T.-Y. Chen, F. Hu, L. Li, S. Ramakrishna, Y. Wu and S. Peng, *J. Am. Chem. Soc.*, 2025, **147**, 33770–33779.

20 J. Yang, K. An, Z. Yu, L. Qiao, Y. Cao, Y. Zhuang, C. Liu, L. Li, L. Peng and H. Pan, *ACS Catal.*, 2024, **14**, 17739–17747.

21 H. Liu, Z. Zhang, J. Fang, M. Li, M. G. Sendeku, X. Wang, H. Wu, Y. Li, J. Ge, Z. Zhuang, D. Zhou, Y. Kuang and X. Sun, *Joule*, 2023, **7**, 558–573.

22 C. Park, S. Ghosh, H. Forbert and D. Marx, *Nat. Commun.*, 2025, **16**(16), 8325.

23 Y. Song, W. Zhao, Z. Wang, W. Shi, F. Zhang, Z. Wei, X. Cui, Y. Zhu, T. Wang, L. Sun and B. Zhang, *J. Am. Chem. Soc.*, 2025, **147**, 13775–13783.

24 W. Yang, Z. Wang, J. Zhang, L. Jia, J. Li, X. Chen, X. Liu, H. Zhang, J. Lin, M. Zhao and Q. Chen, *Angew. Chem., Int. Ed.*, 2025, **64**, e202509768.

25 W. Hu, B. Huang, M. Sun, J. Du, Y. Hai, W. Yin, X. Wang, W. Gao, C. Zhao, Y. Yue, Z. Li and C. Li, *Adv. Mater.*, 2024, **37**, 2411709.

26 Y. Hao, S.-F. Hung, W.-J. Zeng, Y. Wang, C. Zhang, C.-H. Kuo, L. Wang, S. Zhao, Y. Zhang, H.-Y. Chen and S. Peng, *J. Am. Chem. Soc.*, 2023, **145**, 23659–23669.

27 W. C. Liu and F. P. Gabbaï, *Science*, 2024, **385**, 1184–1188.

28 J. Bao, Y. Gu, B. Su, X. Sun, H. Zhang, K. Wang, X. Lin, C. J. Yang, B. Yang, Z. Li, C. L. Dong, Q. Zheng, M. Qiu, L. Lei, C. Yuan, Z. Shao and Y. Hou, *Angew. Chem., Int. Ed.*, 2025, **64**, e202515362.

29 Z. Yu, Z. Wang and X. Gong, *J. Chem. Phys.*, 2025, **163**, 134701.

30 Y. Qiu, M. Sun, J. Wu, C. Chai, S. Wang, H. Huang, X. Zhao, D. Jiao, S. Xu, D. Wang, X. Ge, W. Zhang, W. Zheng, Y. Song, J. Fan, B. Huang and X. Cui, *Nat. Commun.*, 2025, **16**(16), 5262.

31 T. Zhou, X. Li, J. Zhao, L. Luo, Y. Wang, Z. Xiao, S. Hu, R. Wang, Z. Zhao, C. Liu, W. Wu, H. Li, Z. Zhang, L. Zhao, H. Yan and J. Zeng, *Nat. Mater.*, 2025, **24**, 891–899.

32 X. You, B. Xu, H. Zhou, H. Qiao, X. Lv, Z. Huang, J. Pang, L. Yang, P. F. Liu, X. Guan, H. G. Yang, X. Wang and Y.-F. Yao, *ACS Nano*, 2024, **18**, 9403–9412.

33 F. Lin, H. Luo, L. Li, F. Lv, Y. Chen, Q. Zhang, X. Han, D. Wang, M. Li, Y. Luo, K. Wang, L. Gu, Q. Wang, X. Zhao, M. Luo and S. Guo, *Nat. Synth.*, 2024, **4**, 399–409.

34 S. Han, X. Wang, J. Bao, Q. Yang, X. Zeng and D. Cao, *Adv. Funct. Mater.*, 2025, e22524.

35 B. Yuan, Q. Dang, H. Liu, M. G. Sendeku, J. Peng, Y. Fan, L. Cai, A. Cao, S. Chen, H. Li, Y. Kuang, F. Wang and X. Sun, *Nat. Commun.*, 2025, **16**(16), 4583.

36 R. Huang, Y. Wen, P. Miao, W. Shi, W. Niu, K. Sun, Y. Li, Y. Ji and B. Zhang, *Chem Catal.*, 2023, **3**, 100667.

37 J. Wang, K. Liu, W. Liao, Y. Kang, H. Xiao, Y. Chen, Q. Wang, T. Luo, J. Chen, H. Li, T.-S. Chan, S. Chen, E. Pensa, L. Chai, F. Liu, L. Jiang, C. Liu, J. Fu, E. Cortés and M. Liu, *Nat. Catal.*, 2025, **8**, 229–238.

38 C. Tian, R. Liu, Z. Lv, C. Wang, W. Liu, F. Dong, X. Feng, W. Yang and B. Wang, *Adv. Energy Mater.*, 2025, **15**, e01952.

39 T. Lu, J. Li, J. Ying, N. Peng, L. Zhang, Y. Zhang, D. Zhang, S. Ye, L. Xu, D. Sun, H. Li, Y. Gu and Y. Tang, *Adv. Funct. Mater.*, 2024, **35**, 2422594.

40 G. Zhang, J. Pei, Y. Wang, G. Wang, Y. Wang, W. Liu, J. Xu, P. An, H. Huang, L. Zheng, S. Chu, J. Dong and J. Zhang, *Angew. Chem., Int. Ed.*, 2024, **63**, e202407509.

41 Z. Xiao, Y.-C. Huang, C.-L. Dong, C. Xie, Z. Liu, S. Du, W. Chen, D. Yan, L. Tao, Z. Shu, G. Zhang, H. Duan, Y. Wang, Y. Zou, R. Chen and S. Wang, *J. Am. Chem. Soc.*, 2020, **142**, 12087–12095.

42 Y. Mei, J. Chen, Q. Wang and Y. Guo, *Sci. Adv.*, 2024, **10**, eadq6758.

43 Q. Fang, S. Ye, L. Zheng, H. Wang, L. Hu, W. Gu, L. Wang, L. Shi and C. Zhu, *ACS Catal.*, 2024, **14**, 9235–9243.

44 W. Gou, S. Zhang, Y. Wang, X. Tan, L. Liao, Z. Qi, M. Xie, Y. Ma, Y. Su and Y. Qu, *Energy Environ. Sci.*, 2024, **17**, 6755–6765.

45 X. Wang, W. Pi, Y. Qiu, Z. Gong, J. Fan, H. Bao, N. Yao and X. Cui, *Energy Environ. Sci.*, 2025, **18**, 8780–8790.

46 X. Jiang, J. Zhu, M. Jiang, P. Zhang, W. Wen, W. Cai, Y. Ding, P. Sun and M. Cao, *Adv. Mater.*, 2025, **37**, 2503354.

47 F. Qian, D. Cao, S. Chen, Y. Yuan, K. Chen, P. J. Chimtali, H. Liu, W. Jiang, B. Sheng, L. Yi, J. Huang, C. Hu, H. Lei, X. Wu, Z. Wen, Q. Chen and L. Song, *Nat. Commun.*, 2025, **16**(16), 6894.

48 M. Cai, G. Cai, K. Liu, D. Wang, H. Zhao and P. He, *J. Am. Chem. Soc.*, 2025, **147**, 39953–39963.

49 C. Hu, K. Yue, J. Han, X. Liu and L. Liu, *Sci. Adv.*, 2023, **9**, eadf9144.

50 M. Qi, X. Du, X. Shi, S. Wang, B. Lu, J. Chen, S. Mao, H. Zhang and Y. Wang, *J. Am. Chem. Soc.*, 2025, **147**, 18295–18306.

51 L. Deng, H. Chen, S.-F. Hung, Y. Zhang, H. Yu, H.-Y. Chen, L. Li and S. Peng, *J. Am. Chem. Soc.*, 2024, **146**, 35438–35448.

52 Y. Zhang, Y. Yang, P. Meng, J. Yang, H. Shi, X. Chen, X. Lin, D. Fan, S. Chen, D. Wang and Q. Chen, *Small*, 2025, **21**, e06274.

53 C. Yang, Y. Gao, Z. Xing, X. Shu, Z. Zhuang, Y. Wang, Y. Zheng, S. Li, C. Cheng, D. Wang and J. Zhang, *Nat. Commun.*, 2025, **16**(16), 6459.

54 H. Ze, Z.-L. Yang, M.-L. Li, X.-G. Zhang, Y.-L. A, Q.-N. Zheng, Y.-H. Wang, J.-H. Tian, Y.-J. Zhang and J.-F. Li, *J. Am. Chem. Soc.*, 2024, **146**, 12538–12546.

55 J. Huang, R. Wang, H. Sheng, X. Zhu, R. Dominic Ross, D. Hua, L. Lin, Y. Li, Q. Zhang, L. Gu, X. Wang, P. Xu, J. Lu, S. Jiang, J. Han, B. Song and S. Jin, *Nat. Chem.*, 2026, **18**, 669–676.

56 J. Zhu, X. Sun, N. Feng, B. Zhao, M. Qiu, J. Xu and W. Luo, *J. Am. Chem. Soc.*, 2025, **147**, 47454–47466.